Advances in Industrial and Manufacturing Engineering 12 (2026) 100190

Contents lists available at ScienceDirect

Advances in Industrial and Manufacturing Engineering

journal homepage: www.sciencedirect.com/journal/advances-in-industrial-and-manufacturing-engineering

Novel hybrid bobbin tool friction stir welding of AA2219 with comparison to existing bobbin tool variants

Matteo Bernardi [a,*], Ting Chen [a,**], Mikael Guimaraes [a,c], Natã Lucas Beltrão da Silva [a,b], Juliano Marks [a,c], Guilherme N. Rezende [a,b], Pedro Jahn [a,c], Gabriela Gonçalves Gerevini [a,c], Emad Maawad [d], Kai Schimanski [e], Damien Guilloteau [f], Manuel De Araujo [f], Marco Pacchione [g], Luciano Bergmann [a], Benjamin Klusemann [a,h]

[a] Helmholtz-Zentrum Hereon, Institute of Material and Process Design, Solid State Materials Processing, Max-Planck-Str. 1, Geesthacht, 21502, Germany
[b] Federal University of São Carlos, Department of Materials Engineering (DEMa/UFSCar), Rodovia Washington Luiz, km 235, São Carlos, SP, CEP: 13565-905, Brazil
[c] Laboratório de Metalurgia Física, LAMEF, Universidade Federal do Rio Grande do Sul, UFRGS, Porto Alegre, RS, Brazil
[d] Helmholtz-Zentrum Hereon, Institute of Materials Physics, X-Ray Diffraction with Synchrotron Radiation, Max-Planck-Str. 1, Geesthacht, 21502, Germany
[e] Airbus Operations GmbH, Bremen, Germany
[f] Airbus Operations SAS, Toulouse, France
[g] Airbus Operations GmbH, Hamburg, Germany
[h] Leuphana University Lüneburg, Institute for Production Technology and Systems, Universitätsallee 1, Lüneburg, 21335, Germany

ARTICLE INFO

Keywords:
Bobbin tool friction stir welding
Stationary shoulder
WAXS
Mechanical properties
AA2219

ABSTRACT

Bobbin tool friction stir welding (BT-FSW) is a solid-state joining technique that produces high-strength welds without the need for backing plates. This study introduces a new variant, termed hybrid bobbin tool friction stir welding (HBT-FSW), which combines the advantages of conventional BT-FSW and semi-stationary bobbin tool friction stir welding (SSBT-FSW). The HBT-FSW configuration features a probe with a rotating section positioned at the same level as the upper stationary shoulder. This design enhances weld surface quality, while preserving the mechanical performance required for demanding aerospace applications. The process was applied to aluminium alloy AA2219, a common material used in space structures, such as pressurised modules and propellant tanks for orbital systems. A comprehensive microstructural and mechanical characterisation was performed to assess the effectiveness of HBT-FSW. Electron backscatter diffraction (EBSD), hardness mapping, and synchrotron wide-angle X-ray scattering (WAXS) were used to analyse the weld microstructure. Deformation and failure behaviour were investigated through tensile testing with digital image correlation (DIC) and fractographic analysis using scanning electron microscopy (SEM). The results show that HBT-FSW produced a microstructure similar to BT-FSW, achieving comparable tensile strength and ductility while maintaining the superior surface quality typical of SSBT-FSW and enabling welding speeds approximately 30% higher than SSBT-FSW. HBT-FSW therefore represents a promising advancement for the reliable and efficient joining of aluminium alloys in high-performance aerospace structures.

1. Introduction

The rapid evolution of the space industry over recent decades has significantly increased the demand for lightweight, high-performance materials that can withstand extreme service conditions (Henson, 2018). With the increasing push toward commercial launch systems and reusability, the need for materials and joining technologies that balance performance, manufacturability, and durability has become ever more pressing (Wang et al., 2023).

Aluminium alloys remain a material of choice for structural aerospace components, owing to their low density and favourable mechanical properties. Alloys such as AA2219 offer a high strength-to-weight ratio, excellent fatigue resistance, and good stress-corrosion performance (Manikandan et al., 2021). These properties, combined with their

* Corresponding author.
** Corresponding author.
E-mail addresses: matteo.bernardi@hereon.de (M. Bernardi), ting.chen@hereon.de (T. Chen).

https://doi.org/10.1016/j.aime.2026.100190
Received 16 January 2026; Received in revised form 7 April 2026; Accepted 15 April 2026
Available online 23 April 2026

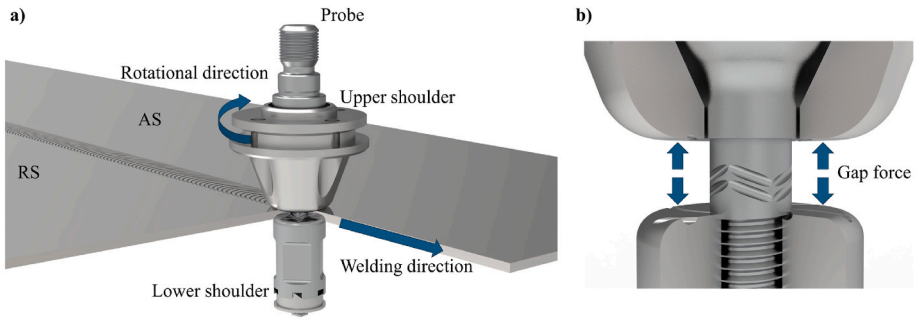

Fig. 1. a) Schematic illustration of the BT-FSW process, in which the presence of a second shoulder eliminates the need for a backing plate. b) Detail showing the gap force between the shoulders during welding.

ability to retain mechanical integrity across a wide temperature range, make them ideal candidates for the fabrication of cryogenic tanks and structural parts in launch vehicles. In fact, AA2219 has been extensively used in legacy systems such as the Saturn V, Space Shuttle, and Ariane 5 (Wang et al., 2018).

Despite these advantages, AA2219 exhibits poor weldability when processed using conventional fusion-based techniques. During fusion welding, the high heat input often leads to solidification defects such as porosity, hot cracking, and microstructural inhomogeneity (Chi et al., 2025). In response to these limitations, friction stir welding (FSW), a solid-state joining technique developed by The Welding Institute (TWI) in 1991, has gained significant attention, particularly in the aerospace sector. The solid-state nature of the process contributes to enhanced weld integrity, minimised distortion, and improved mechanical properties (Mishra and Ma, 2005).

A substantial body of research has focused on FSW of AA2219,

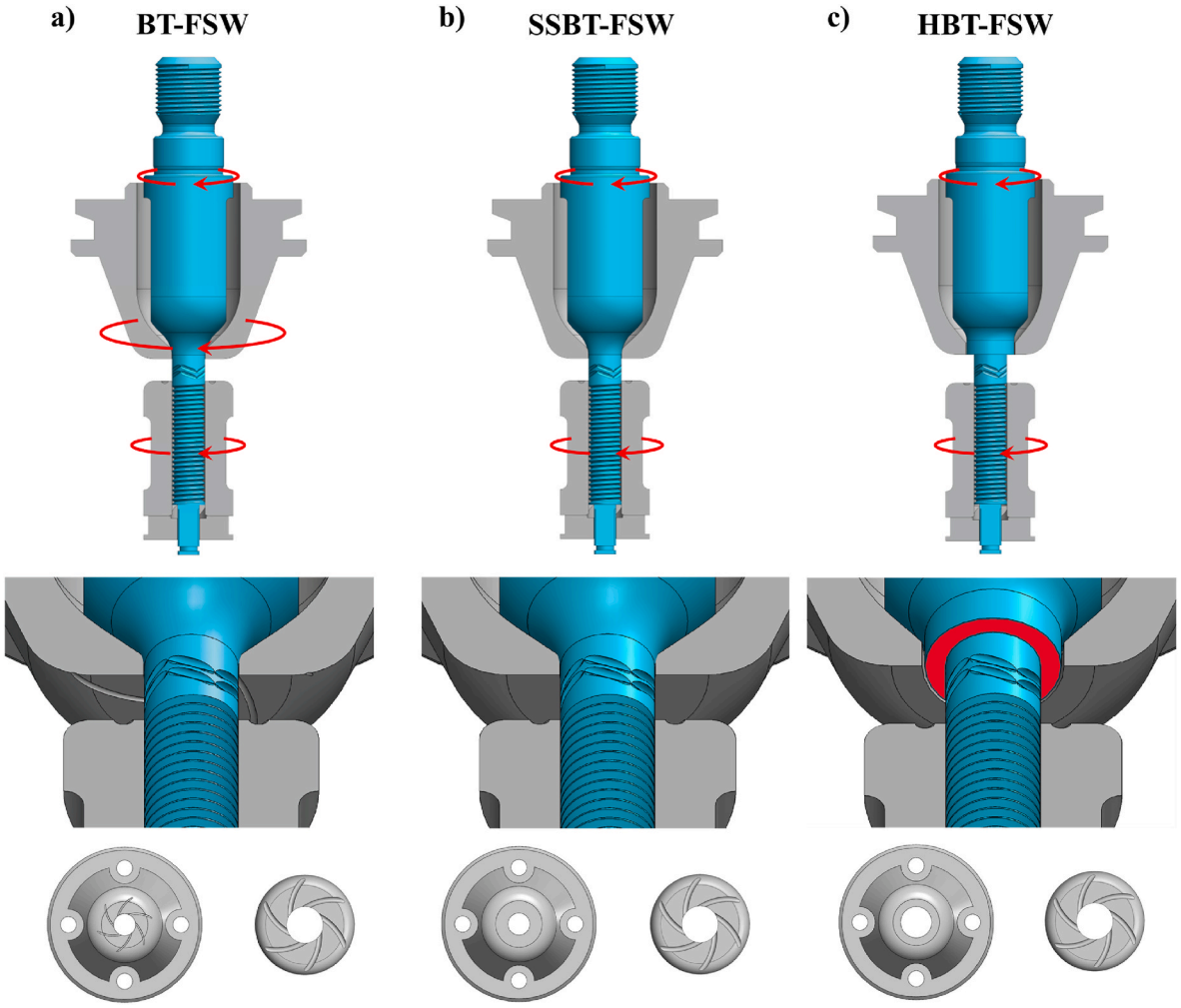

Fig. 2. Schematic representation of the three welding variants employed in this study: a) BT-FSW, with both shoulders and the probe rotating; b) SSBT-FSW, where the upper shoulder remains stationary while the lower shoulder and probe rotate; c) HBT-FSW, in which the upper shoulder is stationary but the probe incorporates a rotating section (highlighted in red) positioned at the same height as the shoulder surface, while the lower shoulder also rotates. For each configuration, the upper row shows a section of the complete tool assembly, with arrows indicating the rotating components. The middle row provides a magnified view of the probe–shoulder region. The bottom row shows the upper and lower shoulders, highlighting the different shoulder designs used in each welding variant.

Table 1
Chemical composition of AA2219-T81 (wt.%), as determined by spark optical emission spectroscopy.

Si	Fe	Cu	Mn	Mg	Cr	Zn	Ti	Zr	V	Sn	Al
0.04	0.10	6.3	0.26	<0.01	<0.01	0.04	0.04	0.09	0.06	0.02	bal

underscoring its critical role in aerospace structures (Wagner et al., 2024). Numerous studies have examined the effects of varying welding parameters on the properties of AA2219 FSW joints (You et al., 2025). Recent advancements have expanded upon these foundations by incorporating advanced process controls, hybrid energy inputs, and considerations for low-temperature performance (Li et al., 2020). For example, Gao et al. (2025) employed a rotating electromagnetic field during FSW of AA2219-T6 to influence microstructural evolution and dynamic recrystallisation behaviour. Additionally, post-weld surface and stress-relief treatments have been demonstrated to further enhance joint performance (Yang et al., 2024). The cryogenic mechanical behaviour of AA2219 FSW joints has also been systematically assessed, confirming their suitability for low-temperature aerospace applications (Hao and Liu, 2022).

Although FSW has been widely adopted by the aerospace industry, its application remains limited to configurations where access is available to position a backing support beneath the joint. This constraint presents significant challenges when welding hollow or closed-section structures, such as fuel tanks, commonly used in aerospace applications. To overcome this limitation, a process variant known as bobbin tool friction stir welding (BT-FSW) was developed. BT-FSW represents a notable advancement in solid-state joining, employing a specially designed tool composed of an upper and lower shoulder connected by a central probe that traverses the full thickness of the workpiece, see Fig. 1 a). This configuration eliminates the need for a backing plate, making the process inherently self-supporting. The welding process can be operated either in gap force-control mode, where the axial force between the shoulders is maintained constant, as shown in Fig. 1 b), or in fixed-gap mode, where the distance between the shoulders is kept constant throughout welding.

Recent investigations have provided valuable insight into the process–structure–property relationships of this configuration. Li et al. (Wang et al., 2022) reported that defect formation and microstructural evolution in BT-FSW of AA2219-T8 are strongly governed by tool geometry and process parameters. These factors control energy input and the stability of material flow, ultimately determining joint strength and integrity. Complementary studies on the microstructure and corrosion behaviour in BT-FSW of AA2219 have shown that the refined grain structure and redistributed precipitates in the stir zone improve corrosion resistance relative to conventional FSW joints (Shao et al., 2022). More recently, Rezende et al. (2025) demonstrated that post-weld heat treatment significantly enhances the mechanical properties of these joints. Collectively, these studies confirm the strong potential of bobbin tool configurations for producing high-integrity AA2219 welds suitable for aerospace applications.

Further advancements in BT-FSW have aimed to improve mechanical properties and surface quality through the development of tool designs featuring stationary elements. This approach is known as semi-stationary bobbin tool friction stir welding (SSBT-FSW). In this configuration, the lower shoulder and probe rotate while the upper shoulder remains stationary, see Fig. 2 b). The stationary upper shoulder induces an ironing effect that smooths the weld surface and avoids flash formation (Li et al., 2023). Although this configuration is known to produce excellent external surface quality and improved mechanical properties, having only one of the two shoulders rotating results in reduced energy input on the upper surface (Wu et al., 2015). As a consequence, lower welding speeds might be required to ensure defect-free welds.

Building upon the advantages of both conventional and semi-stationary designs, the present study introduces a novel hybrid bobbin tool friction stir welding (HBT-FSW) configuration. In this design, the upper shoulder remains stationary, while the probe incorporates a flat rotating element positioned coplanar with the shoulder surface, see Fig. 2 c). This hybrid design allows the upper weld surface to benefit from the local stirring and thermal input of a rotating element, while maintaining the surface quality associated with stationary shoulder configurations.

The performance of this novel hybrid configuration is evaluated against two established BT-FSW configurations: the conventional fully rotating bobbin tool and the semi-stationary shoulder variant. A comprehensive assessment of the welds is conducted through microstructural characterisation, hardness profiling, surface morphology, and mechanical testing to demonstrate the potential advantages of this novel approach for aerospace applications.

Table 2
Mechanical properties of AA2219-T81.

Ultimate tensile strength (MPa)	Yield strength (MPa)	Elongation (%)	Hardness ($HV_{0.1}$)
455.1 ± 0.1	367.5 ± 2.2	10.35 ± 1.31	147 ± 1

2. Materials and methods

2.1. Material and welding setup

AA2219-T81 aluminium alloy sheets, with dimensions of 1000 × 150 × 3 mm (length × width × thickness), were welded in a butt-joint configuration using three process variants: BT-FSW, SSBT-FSW, and HBT-FSW. The chemical composition of the base material is provided in Table 1. The base material was supplied in the T81 temper, corresponding to solution heat treatment, cold working, and artificial ageing, resulting in a high density of finely dispersed θ′ precipitates that provide the primary strengthening mechanism. The mechanical properties of AA2219-T81, summarised in Table 2, were obtained from tensile testing of three samples in accordance with DIN 50125 and Vickers hardness measurements were performed according to ISO 6507-1. Prior to welding, the sheet surfaces were cleaned with ethanol to remove surface contaminants. The edges were then milled to ensure a precise and parallel joint line. A mechanical clamping fixture was employed to prevent sheet movement during welding.

A customised weld head was integrated into a PKM T805 five-axis parallel kinematic robotic platform (Loxin, Spain) to carry out the joining operations. All welds were executed in gap force-controlled mode, where the axial force between the two tool shoulders was kept constant throughout the process.

The welding tool used in all configurations was equipped with a 7 mm diameter probe, and both the upper and lower shoulders featured a flat contact area 15 mm in diameter. The probe was fabricated from MP159, a high-strength nickel–cobalt-based superalloy, while the shoulders were manufactured from X38CrMoV5-1 chromium–molybdenum–vanadium hot work tool steel. The probe has zig-zag shaped features to enhance stirring and mixing within the plasticised material. The lower shoulder incorporated radially symmetric, equally spaced spiral features designed to promote material flow. In the SSBT-FSW and HBT-FSW configurations, the upper shoulder was smooth and stationary, while in the BT-FSW configuration, it featured equally spaced spiral patterns similar to those on the lower shoulder. Additionally, in the HBT-FSW configuration, the probe included a 10 mm diameter section that rotated at the same level as the upper stationary

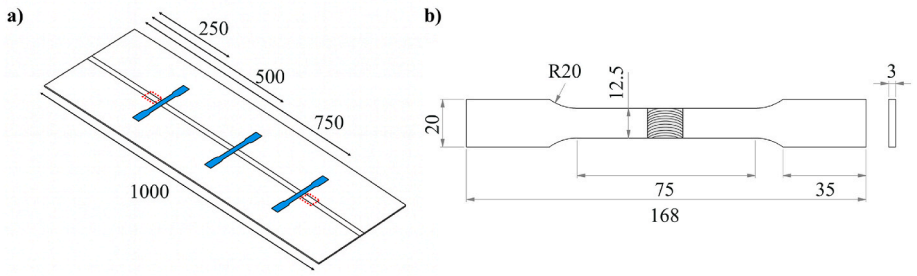

Fig. 3. a) Schematic illustrating the selected regions for the extraction of specimens used for tensile testing; the dashed red area indicates the region where X-ray radiographic inspections were performed. b) Dimensions of the tensile test specimens. All dimensions in mm.

Fig. 4. Macrograph of the SSBT-FSW joint produced at a welding speed of 200 mm/min, showing the presence of a surface defect on the advancing side. Therefore, for SSBT-FSW a lower welding speed of 150 mm/min was chosen in this study.

shoulder, see Fig. 2 c). This section was featureless, and both the probe and the shoulder exhibited a surface roughness of approximately Rz 25 µm. At the probe–shoulder interface, the upper shoulder thickness was 3 mm for all the variants.

For microstructural characterisation, rectangular specimens (45 × 20 mm) were extracted from the weld centreline. X-ray radiography was employed to inspect the welds over extended regions and assess the presence of internal defects, as shown in Fig. 3 a). X-ray radiography was performed using a Y.Cougar SMT system (YXLON International GmbH, Germany), operated at an accelerating voltage of 100 kV and a current of 120 µA. Defects on the order of 1 µm were detectable under the applied inspection conditions.

Tensile specimens according to ISO 4136 were prepared from three distinct locations along the weld length: near the start (250 mm from the leading edge), the middle (500 mm), and the end (750 mm), as shown in Fig. 3 a). The dimensions of the tensile specimens are provided in Fig. 3 b). All specimens were kept at room temperature for four weeks before mechanical and hardness testing to ensure that natural ageing processes had stabilised.

Temperature measurements were carried out using type K thermocouples (Conatex, Germany) at a sampling frequency of 10 Hz. The thermocouples were inserted into 0.6 mm diameter holes located at mid-thickness, positioned 15 mm from the butt joint and approximately 500 mm along the weld length. For the HBT-FSW and SSBT-FSW configurations, additional thermocouples were placed on the upper shoulder at a distance of 1 mm from the probe-shoulder interface.

The welding parameters were optimised in collaboration with the project's industrial partner, with a target welding speed of 200 mm/min. However, for the SSBT-FSW configuration, a reduced welding speed of 150 mm/min was adopted for this study, as defect-free welds could not be achieved at 200 mm/min, see Fig. 4. These defects are located on the upper surface and can be attributed to insufficient heat input beneath the stationary shoulder at higher welding speeds. In the SSBT-FSW configuration, the absence of a rotating shoulder reduces heat generation at the surface, leading to defect formation at higher welding speeds. This is supported by the temperature measurements at the upper shoulder, which reach only ~375 °C for SSBT-FSW at 200 mm/min, compared to ~400 °C for SSBT-FSW at 150 mm/min and ~475 °C for HBT-FSW at 200 mm/min.

Accordingly, the final parameters selected for all configurations were a rotational speed of 400 rpm and a constant gap force of 5 kN for all configurations, with a welding speed of 200 mm/min for BT-FSW and HBT-FSW and 150 mm/min for SSBT-FSW.

2.2. *Weld characterisation methods*

Metallographic characterisation was performed on cross-sectional specimens extracted from the welds. Samples were mounted, ground, and polished according to standard metallographic procedures, followed by electrochemical etching in Barker's reagent for 70 s at 25 V using a LectroPol-5 system (Struers, Denmark). The resulting microstructure was examined using an optical microscope (DM2700, Leica Microsystems, Germany).

Grain size was evaluated by electron backscatter diffraction (EBSD). Specimens underwent final surface preparation by vibratory polishing using a VibroMet 2 machine (Buehler, Germany) with a 0.02 µm colloidal silica suspension. EBSD characterisation was performed using a Quanta 650 FEG scanning electron microscope (Thermo Fisher Scientific, USA) equipped with an EDAX Velocity EBSD detector and an EDAX Apollo X EDS system (AMETEK Inc., USA). Data were acquired with a step size of 0.5 µm and processed using TSL OIM Analysis™ v8 software. EBSD scans were focused on the centre of the weld at mid-thickness. Recrystallised grains were identified based on the grain orientation spread (GOS) obtained from EBSD analysis. Grains with a GOS below 2° were classified as recrystallised, those with GOS values between 2° and 5° were considered to contain substructure, and grains with higher GOS values were categorised as deformed.

Surface topography was characterised using a Keyence VR Series profilometer, which provides high-resolution three-dimensional surface mapping with a lateral resolution of 0.1 µm. These measurements were employed to evaluate weld surface features, including flash formation and surface smoothness.

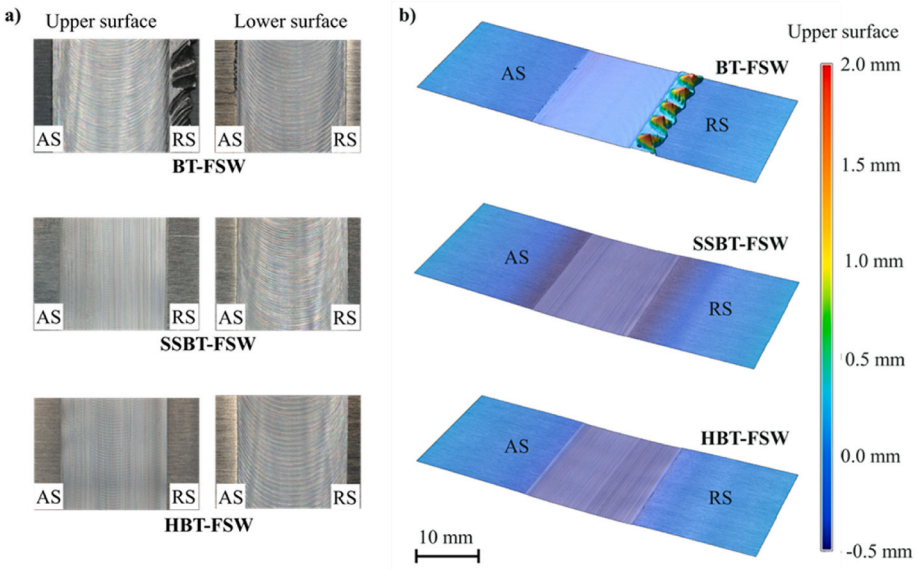

Fig. 5. a) Surface appearance of the upper and lower surfaces for the three welding variants. b) Three-dimensional surface topography maps, obtained by profilometry, comparing the upper surfaces. HBT-FSW achieves a smooth, flash-free surface comparable to SSBT-FSW.

Vickers microhardness measurements were conducted using a DuraScan 70 G5 system (EMCO-Test Prüfmaschinen GmbH, Germany), equipped with a 136° pyramidal indenter. A load of 0.1 kg (HV0.1) was applied, with indentations spaced 0.25 mm apart along a transverse line positioned at the mid-thickness of the weld, normal to the welding direction.

Wide-angle X-ray scattering (WAXS) measurements were performed. The beam energy was set to 87.1 keV, and a two-dimensional PerkinElmer flat-panel detector (2048 × 2048 pixels, 200 × 200 μm^2 pixel size) was employed to record the Debye–Scherrer rings. The incident beam had a cross-section of 0.5 × 0.5 mm^2. The sample–detector distance, calibrated using a LaB_6 standard powder, was approximately 1.498 m. Measurements were carried out along the samples with a step size of 0.5 mm over a total length of 45 mm, using the same specimens tested for hardness to enable a direct correlation between microstructural and mechanical data. The two-dimensional diffraction patterns were integrated using Pydidas (Storm and Lotze, 2025). The strongest reflections of the Al_2Cu-based precipitates, specifically, the (101) peak of the metastable θ′ phase and the (110) peak of the equilibrium θ phase, were analysed using multi-phase Rietveld refinement of the integrated diffraction patterns in the Materials Analysis Using Diffraction (MAUD) software (Chan et al., 2025). Peak separation between the θ′ and θ phases was achieved using their respective crystallographic models with constrained structural parameters. The background was modelled with a polynomial function with six coefficients, and peak profiles were described using a pseudo-Voigt function accounting for both Gaussian and Lorentzian broadening contributions. The quality of the refinements was evaluated using the R_{wp}, which remained below 10% for all

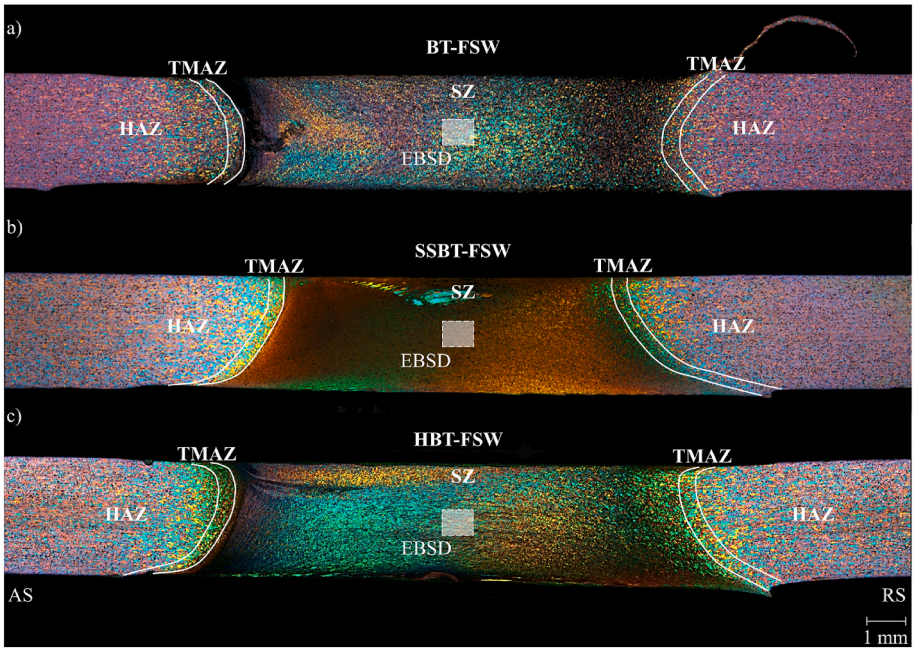

Fig. 6. Macrographs of weld cross-sections for a) BT-FSW, b) SSBT-FSW, and c) HBT-FSW joints, obtained by optical microscopy. The main weld regions (SZ, TMAZ, and HAZ) are indicated. The regions selected for EBSD analysis are indicated by the white dashed boxes.

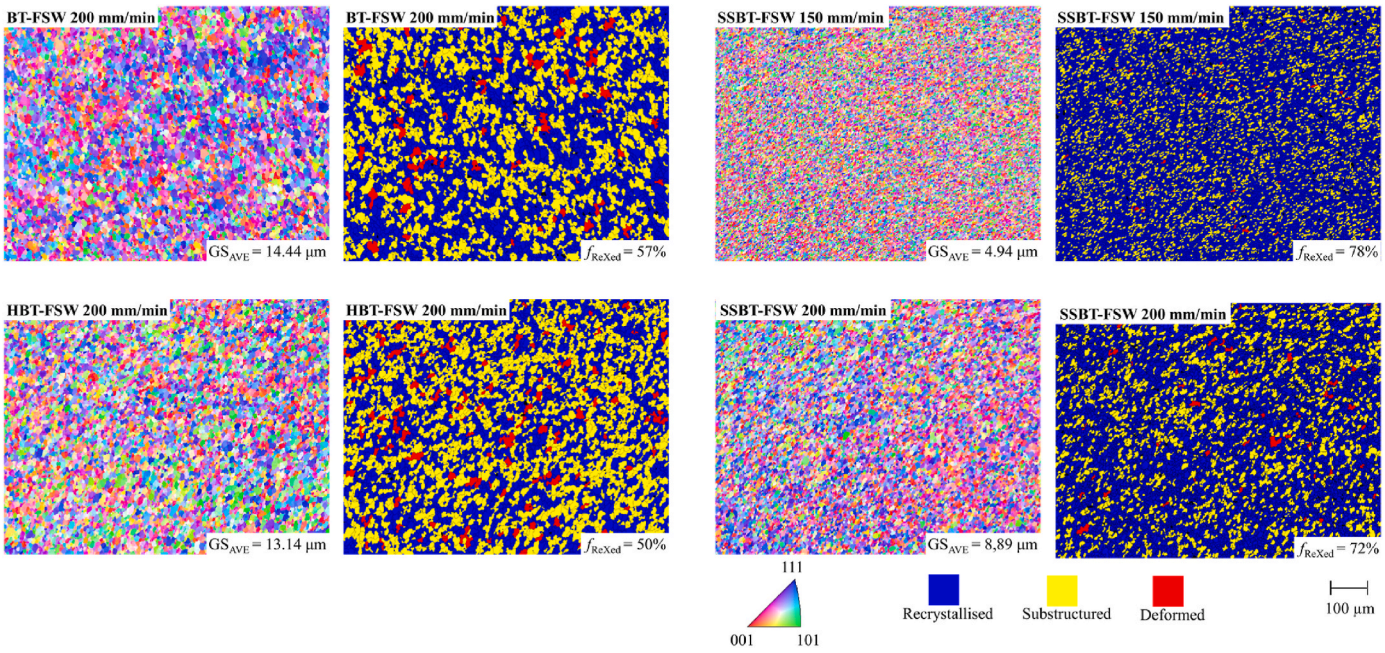

Fig. 7. Inverse pole figure (IPF) and corresponding GOS maps at the mid-thickness of the SZ for the different welding conditions. BT-FSW and HBT-FSW were welded at 200 mm/min, while SSBT-FSW was performed at 200 and 150 mm/min; the reduced welding speed was used to avoid surface defects. The average grain size (GS_{AVE}) is indicated in the IPF maps, while the fraction of recrystallised material (f_{ReXed}) is reported in the GOS maps.

analysed positions, see Fig. S1. These values indicate good agreement between experimental and calculated patterns (Ramkumar et al., 2018).

Tensile testing was conducted using a Z100 universal testing machine (ZwickRoell, Germany) fitted with a 50 mm clip gauge (MTS Systems, USA) at a crosshead speed of 1 mm/min. Local strain distributions were analysed via DIC, utilising a stereo-camera system (ARAMIS, GOM GmbH) to acquire full-field strain maps. The resulting data were subsequently processed using ARAMIS Professional 2023 software.

3. Results and discussion

3.1. Surface morphology

Surface analysis revealed that the upper shoulder design has a pronounced effect on weld appearance, while the lower shoulder, which was identical in all configurations, produced a comparable surface finish across the three variants, as shown in Fig. 5(a). In conventional BT-FSW, micro-grooves generated by the rotating upper shoulder are observed on the upper surface, along with moderate flash formation. In contrast, the SSBT-FSW configuration produced an exceptionally smooth surface due to the ironing effect of the stationary upper shoulder. Notably, the HBT-FSW variant achieved a similarly smooth finish; despite incorporating a rotating insert, its upper surface remained free from the characteristic micro-grooves of BT-FSW, as shown in Fig. 5(b). A larger area of the upper surface for all investigated welds is provided in Fig. S2.

In BT-FSW, micro-grooves and flashes can reduce fatigue life and necessitate post-weld machining prior to the application of protective coatings or surface treatments (Gong et al., 2025). The significant removal of surface irregularities achieved by SSBT-FSW and HBT-FSW is therefore expected to decrease sensitivity to surface crack initiation and to enhance fatigue performance (Zhang et al., 2023). The HBT-FSW configuration's ability to combine the welding speed of BT-FSW with the superior surface finish characteristic of SSBT-FSW represents a considerable advantage for industrial implementation.

3.2. Microstructure

The macrographs of the cross-sections for the BT-FSW, SSBT-FSW, and HBT-FSW welds are shown in Fig. 6. All welds indicate no evidence of internal defects. The overall shape of the stir zone (SZ) varied with the tool configuration. The BT-FSW joint exhibits the typical hourglass shape produced by the symmetrical action of the two rotating shoulders. In the SSBT-FSW weld, the SZ appears asymmetrical, widening towards the rotating lower shoulder, with the upper part of the SZ being narrower because of the absence of rotation at the stationary shoulder. The HBT-FSW weld displays an intermediate geometry. The rotating insert of the probe positioned at the height of the stationary shoulder improved material flow at the upper surface, leading to an hourglass profile while maintaining the smooth surface quality typical of the stationary shoulder configurations. In all cases, the macrostructure consists of the expected zones: a central SZ, surrounded by the thermo-mechanically affected zone (TMAZ), and the heat-affected zone (HAZ) transitioning into the base material (BM).

The TMAZ exhibits elongated and deformed grains, with a sharper boundary to the SZ on the advancing side (AS) and a more gradual transition on the retreating side (RS). This asymmetry is typical of friction stir welding and results from differences in material flow and temperature between the two sides. Similar behaviour has been reported in FSW of aluminium alloys, where higher strain rates and temperature gradients on the AS arise from the more intense shearing action of the rotating probe (Cabibbo et al., 2007). The HAZ was influenced only by the thermal cycle and retained the elongated grain structure of the BM.

X-ray inspection (Fig. S3) further confirmed the absence of volumetric defects in BT-FSW, SSBT-FSW at 150 mm/min, and HBT-FSW, whereas defects were detected in SSBT-FSW at 200 mm/min.

EBSD analysis revealed that all welds developed a recrystallised, fine-grained structure within the SZ as a result of severe plastic deformation and frictional heating, see Fig. 7. To enable a clearer correlation between welding parameters, process variants, and microstructural evolution, EBSD was also performed on the SSBT-FSW joint welded at 200 mm/min, even though this condition exhibited surface defects. In all welding conditions, the mean grain size in the SZ is significantly smaller than that of the BM, confirming that dynamic recrystallisation is the dominant restoration mechanism (Jata and Semiatin, 2000). At a welding speed of 200 mm/min, both BT-FSW and HBT-FSW joints exhibit similar average grain sizes, whereas the SSBT-FSW configuration

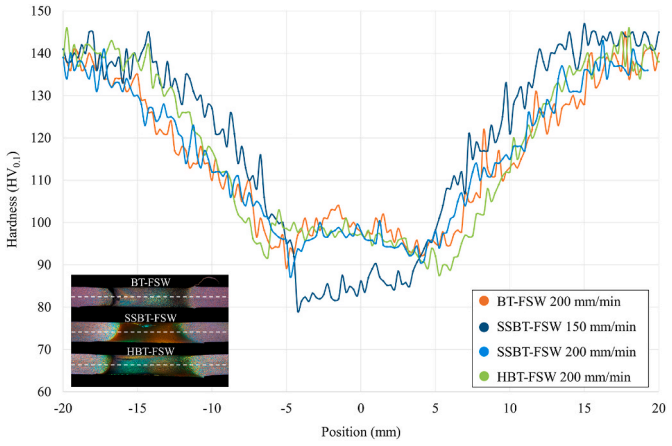

Fig. 8. Microhardness profiles ($HV_{0.1}$) measured at mid-thickness across the weld cross-section for BT-FSW, SSBT-FSW, and HBT-FSW joints. Results are shown for BT-FSW and HBT-FSW welded at 200 mm/min, and for SSBT-FSW welded at 150 and 200 mm/min.

produces a finer microstructure. This observation is consistent with the GOS analysis shown in Fig. 7, which reveals a higher fraction of recrystallised grains (f_{ReXed}) in SSBT-FSW (~72%) compared to BT-FSW (~57%) and HBT-FSW (~50%) at the same welding speed, indicating a more extensive recrystallisation of the stir zone in SSBT-FSW at the same welding speed. At a reduced welding speed of 150 mm/min in SSBT-FSW (to avoid surface defects), an additional grain refinement is observed, with the GOS data indicating a recrystallised fraction of approximately 78%.

The microhardness profiles measured at mid-thickness for the different welding conditions are shown in Fig. 8. Microhardness measurements were also carried out on the SSBT-FSW joint welded at 200 mm/min, in order to better distinguish the effect of welding speed from that of the process variant. All welding variants resulted in a reduction in joint hardness compared to the BM. At a welding speed of 200 mm/min, the SSBT-FSW joint exhibits hardness levels comparable to those of the BT-FSW and HBT-FSW joints across the weld cross-section. In contrast, when the welding speed in the SSBT-FSW configuration is reduced to 150 mm/min to avoid surface defects, a decrease in hardness is observed within the SZ. The reduced hardness observed for the SSBT-FSW joint welded at 150 mm/min cannot be attributed to grain size effects, as this condition exhibits the finest recrystallised grains, which would normally increase hardness according to the Hall–Petch relationship (Keerti et al., 2025). Instead, the hardness reduction originates from changes in the precipitation state caused by the prolonged thermal exposure associated with the reduced welding speed in the SSBT-FSW configuration. The semi-stationary variant also shows a comparatively narrower hardness profile, in agreement with the reduced stir zone width revealed by macrostructural analysis. This confirms that the observed hardness reduction is primarily governed by welding speed rather than tool configuration alone.

The mechanical behaviour of AA 2219 is governed by its precipitation-hardening response, which results from a well-defined sequence of metastable phases derived from the supersaturated solid solution (Miyoshi et al., 2021). Age hardening begins with the formation of Guinier–Preston (GP) zones, followed by the development of θ'' and θ' precipitates and, ultimately, the equilibrium θ phase (Reimann et al., 2018). The accepted precipitation sequence for AA 2219 can be expressed as (Perrin et al., 2025):

SSSS → GP(I) zones → θ'' (GP(II) zones) → θ' → θ

The θ″ phase, which is fully coherent with the aluminium matrix, forms during early ageing and provides a significant strengthening effect through coherency strain hardening. As ageing progresses, θ″ transforms into the semi-coherent θ′ phase, which dominates in the peak-aged

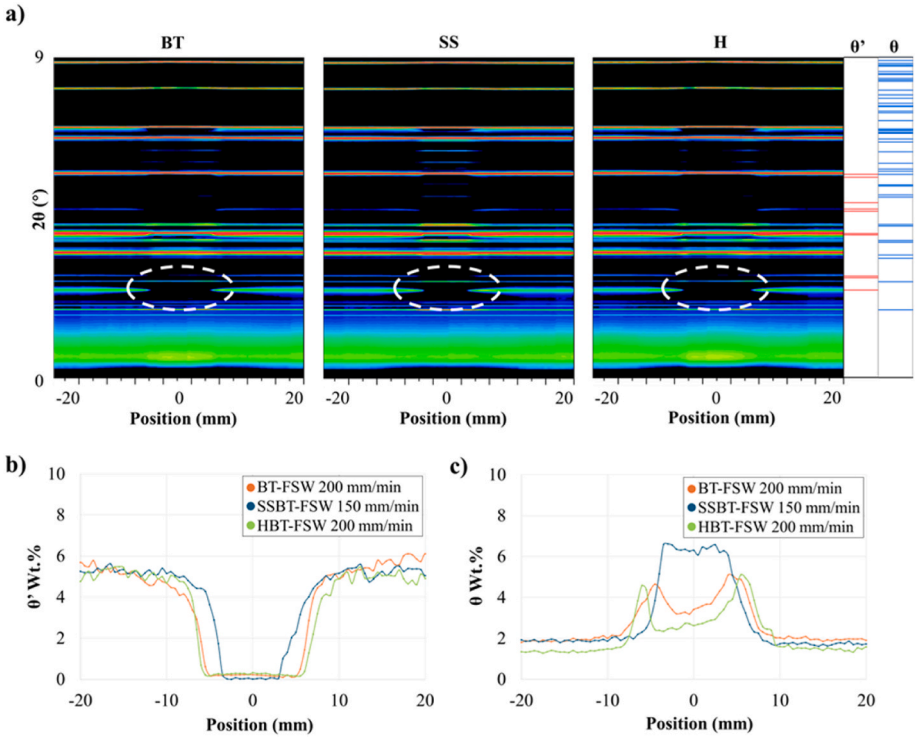

Fig. 9. Comparative microstructural analysis of BT-FSW, SSBT-FSW, and HBT-FSW joints. The SSBT-FSW joint was welded at 150 mm/min to avoid surface defects, while the BT-FSW and HBT-FSW joints were welded at 200 mm/min a) Synchrotron WAXS intensity maps showing the spatial distribution of diffraction signals across the welds; the dashed ellipses highlight the SZ regions. The Bragg peak positions of the θ and θ′ phases, calculated using the corresponding ICDD PDF data and literature values (Wang and Starink, 2005), are also shown. b) and c) show the evolution of the weight fraction of the θ′ phase and θ phase across the welds.

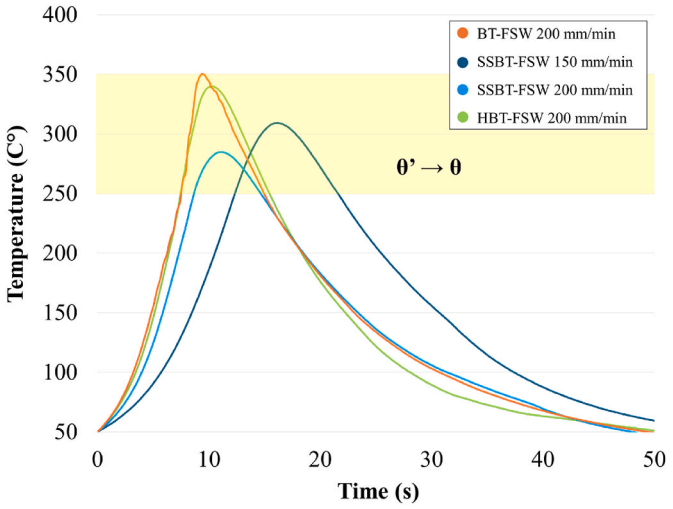

Fig. 10. Temperature evolution during welding for the different process conditions (BT-FSW, SSBT-FSW, and HBT-FSW). The highlighted region indicates the temperature range associated with the θ′ → θ transformation (~250–350 °C). The SSBT-FSW condition at 150 mm/min exhibits the longest exposure within this temperature range.

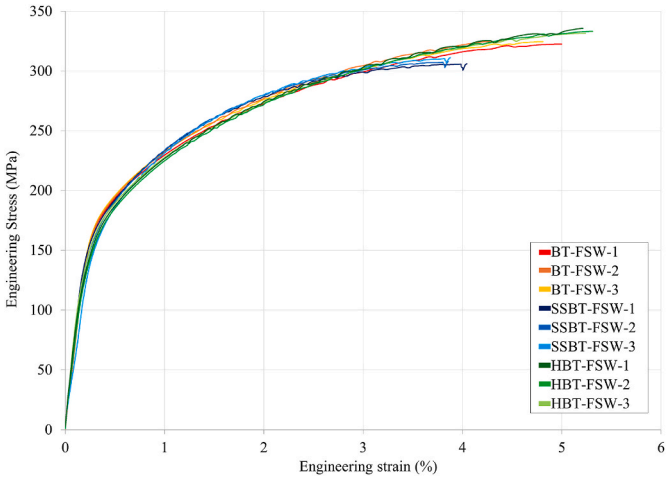

Fig. 11. Engineering stress–strain curves for the three welding variants (BT-FSW and HBT-FSW welded at 200 mm/min, SSBT-FSW welded at 150 mm/min), each tested three times at a constant crosshead speed of 1 mm/min.

condition (Stobbs and Purdy, 1978). The θ precipitates, in contrast, are stable and incoherent. Due to their typically large size and low aspect ratio, they exert little to no hardening effect on the alloy (Wolverton and Ozoliņš, 2001).

The temperature evolution during welding provides further insight into the observed microstructural and mechanical differences, as shown in Fig. 9. The SSBT-FSW condition at 150 mm/min exhibits both a higher peak temperature and a significantly broader thermal cycle compared to the other conditions, indicating prolonged exposure within the temperature range associated with θ′ → θ transformation. In contrast, the SSBT-FSW condition at 200 mm/min and the BT-FSW and HBT-FSW conditions show shorter thermal cycles with reduced high-temperature exposure.

To clarify this behaviour, synchrotron WAXS was performed across the welds without defects. The technique was used to identify the θ′ and θ phases and to assess their evolution within the different welding variants. The phase weight fractions were determined by Rietveld refinement.

The WAXS intensity maps for the three variants are shown in Fig. 9 a), where the SZ is highlighted by dashed ellipses. From the maps, it is evident that the Bragg reflections corresponding to the θ′ and θ phases undergo pronounced changes within the SZ compared with the BM. All welds show a reduction in the θ′ weight fraction in the vicinity of the SZ, indicating a decrease in the amount of this strengthening phase due to partial dissolution or transformation during welding, as shown in Fig. 9 b). Simultaneously, an increase in the θ phase weight fraction is observed in all cases, suggesting that a fraction of θ′ transforms into the equilibrium θ phase. Among the investigated configurations, the SSBT-FSW weld (150 mm/min) exhibits the most pronounced increase in θ weight fraction, indicating that the longer thermal exposure associated with the reduced welding speed promotes more extensive θ′→θ transformation, as shown in Fig. 9 c). The reduced welding speed required in the SSBT-FSW configuration prolongs the thermal exposure of the material, thereby promoting more extensive θ′→θ transformation. The metastable nature of θ′ precipitates makes their growth and transformation into the equilibrium θ phase highly temperature dependent; when exposed to temperatures above roughly 250 °C (Jiang et al., 2021), rapid coarsening and transformation to θ take place, leading to over-ageing and a consequent reduction in strength. In contrast, the BT-FSW and HBT-FSW joints exhibit a less pronounced θ′→θ transformation, reflected by the lower θ weight fractions, indicating a reduced extent of over-ageing within the SZ compared to SSBT-FSW.

The temperature evolution during welding provides further insight into these observations. As shown in Fig. 10, the SSBT-FSW condition at 150 mm/min does not exhibit the highest peak temperature, but shows the longest exposure within the temperature range associated with θ′ → θ transformation (above ~250 °C). The time spent above this threshold is approximately 9.4 s for SSBT-FSW at 150 mm/min, compared to 5.9 s for SSBT-FSW at 200 mm/min, and 7.3 s and 7.8 s for BT-FSW and HBT-FSW at 200 mm/min, respectively. This prolonged exposure promotes enhanced precipitate coarsening and transformation of θ′ into θ, explaining the higher θ fraction observed by WAXS for the SSBT-FSW condition at 150 mm/min.

In AA2219, strength is mainly attributed to the precipitation strengthening of θ′ precipitates (Chen et al., 2025), with additional contributions from dislocation density and grain structure. The present results show that precipitation evolution is the dominant factor controlling hardness in the present welds.

In particular, the SSBT-FSW condition at 150 mm/min exhibits the lowest hardness despite having the finest grain structure, while the SSBT-FSW condition at 200 mm/min shows hardness comparable to BT-FSW and HBT-FSW despite a higher fraction of recrystallised grains. These observations confirm that grain size and dislocation-related strengthening are not the primary factors governing the hardness variation in this study.

Instead, the hardness evolution correlates directly with the precipitation state. The WAXS results (Fig. 9) show a more pronounced reduction in θ′ phase fraction and a corresponding increase in θ phase fraction for the SSBT-FSW condition at 150 mm/min, indicating enhanced transformation and coarsening of strengthening precipitates. This is consistent with the thermal measurements, which show a longer exposure above ~250 °C, promoting θ′ dissolution and transformation.

3.3. *Quasi-static properties and fracture analysis*

Tensile testing was performed on the welds without defects. All three welding variants exhibited comparable mechanical behaviour, with BT-FSW and HBT-FSW showing a yield strength equal to or above 180 MPa, an ultimate tensile strength (UTS) exceeding 320 MPa, and an elongation of around 5 %. SSBT-FSW showed slightly lower performance, with an elongation of approximately 4 % and marginally reduced UTS, originating primarily from the lower welding speed required to avoid surface defects. Each variant was tested three times and all specimens showed highly consistent stress–strain curves (Fig. 11), confirming that the mechanical properties are uniform along the weld length. The

Table 3
Yield strength, UTS, and elongation for the three welding variants, as determined from tensile tests.

Condition	Yield Strength (MPa)	UTS (MPa)	Elongation (%)
BT-FSW (200 mm/min)	191.2 ± 1.7	324.9 ± 2.6	4.8 ± 0.2
SSBT-FSW (150 mm/min)	187.4 ± 4.7	308.3 ± 2.6	3.9 ± 0.1
HBT-FSW (200 mm/min)	180.8 ± 2.0	333.4 ± 2.1	5.3 ± 0.1

average mechanical properties obtained from the tests are summarised in Table 3.

DIC provided further insight into the localised deformation behaviour during tensile loading, see Fig. 12. For all configurations, strain was observed to concentrate preferentially on the AS. The sharp transition between the SZ and TMAZ serves as a site of local stress concentration due to the microstructural mismatch, with failure frequently initiating from this region under mechanical loading (Cabibbo et al., 2007). SSBT-FSW exhibited a larger area of high local strain, attributed to the combined effects of microstructural mismatch at the SZ/TMAZ transition and higher precipitate degradation within the SZ, as identified by WAXS, compared with the other two variants. It is interesting to note

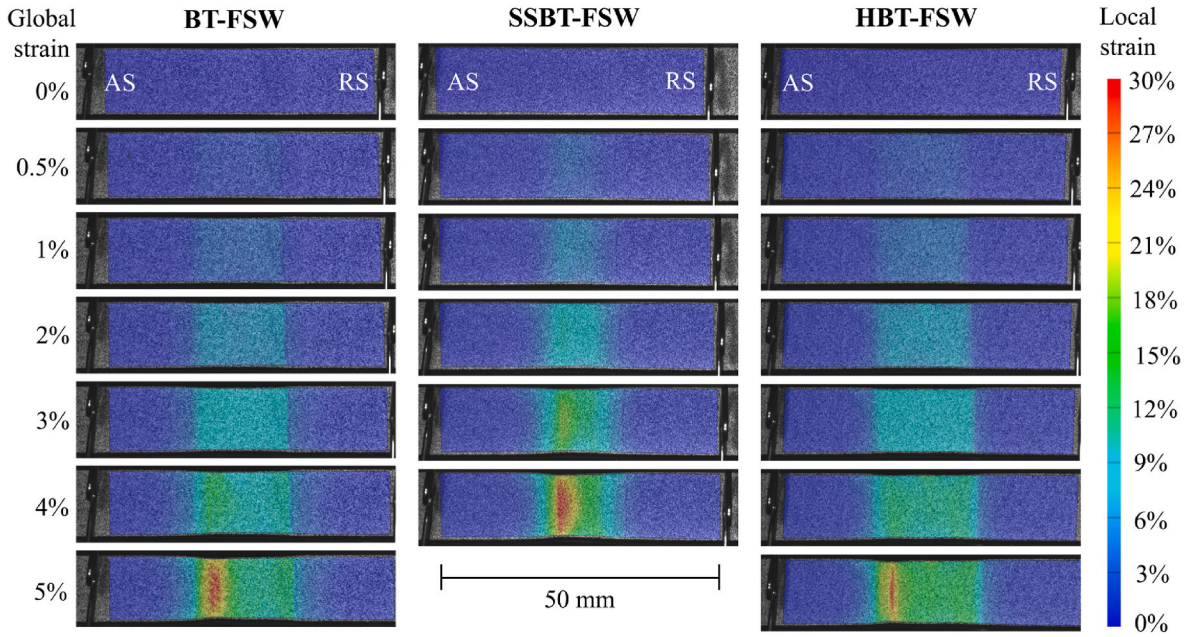

Fig. 12. In situ extensional strain distribution for the three welding variants, obtained using DIC. SSBT-FSW failed at approximately 4% global strain, while BT-FSW and HBT-FSW failed at around 5%.

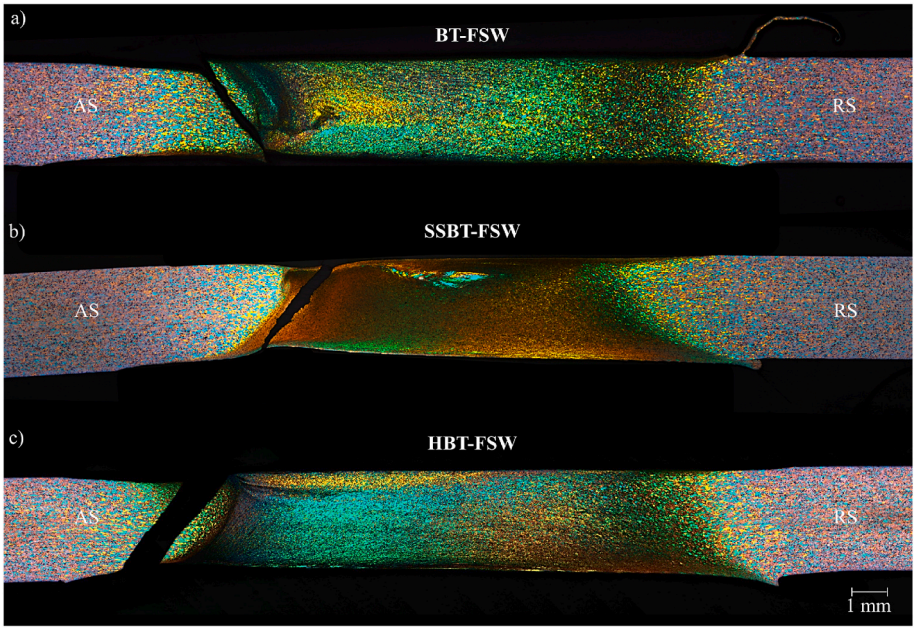

Fig. 13. Fracture locations for (a) BT-FSW, (b) SSBT-FSW, and (c) HBT-FSW joints. Fracture occurred within the SZ for SSBT-FSW, whereas BT-FSW and HBT-FSW failed at the transition between SZ and TMAZ.

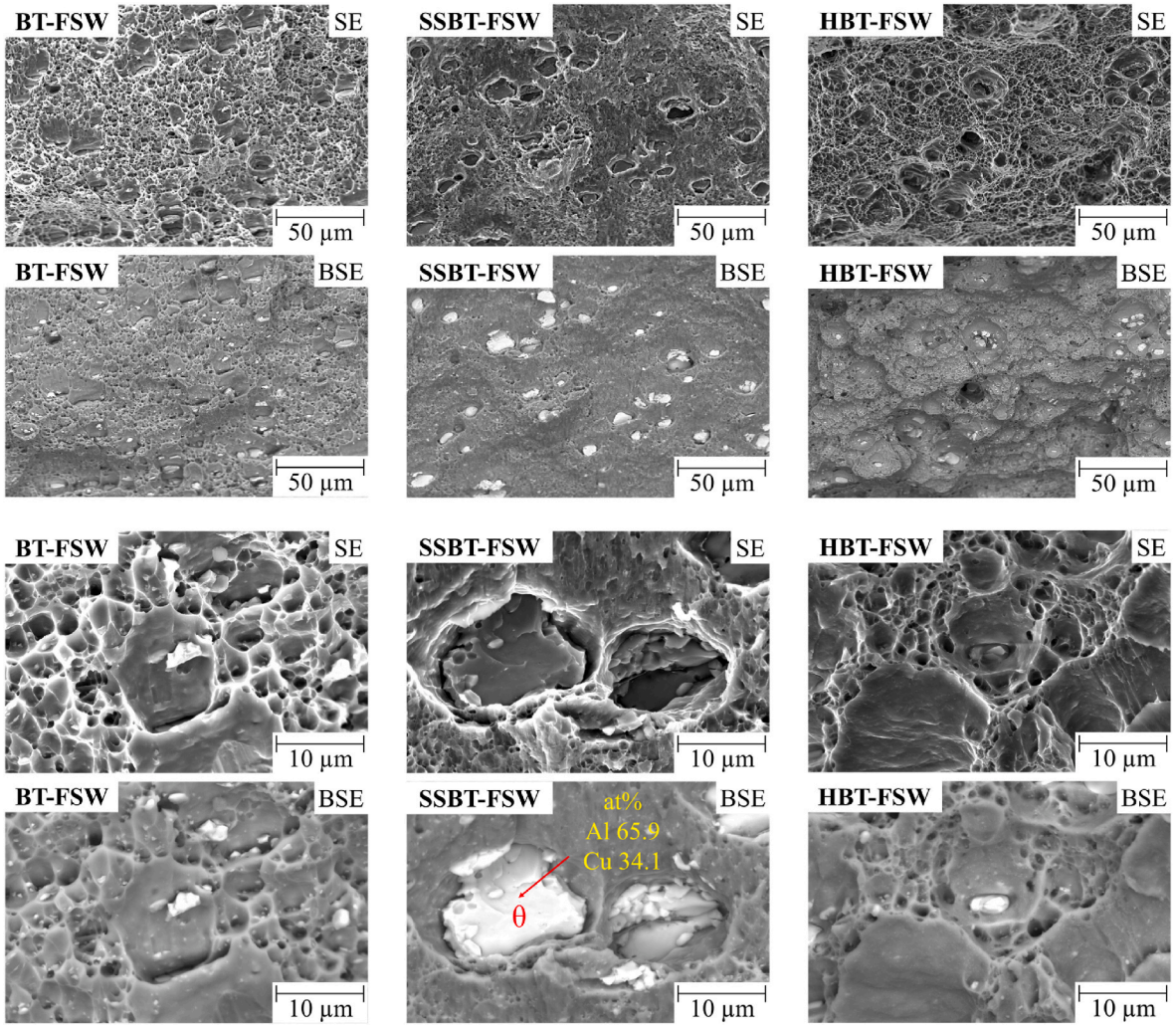

Fig. 14. SEM micrographs of the fracture surfaces for the three welding variants at various magnifications, including secondary electron (SE) images for surface morphology and backscattered electron (BSE) images for compositional contrast. SSBT-FSW (150 mm/min) shows fewer and shallower dimples than BT-FSW and HBT-FSW, consistent with its lower elongation at fracture. BSE imaging combined with EDS analysis identifies Al_2Cu (θ) particles as void nucleation sites, supporting the observed reduction in ductility for SSBT-FSW.

that in BT-FSW the characteristic surface microgrooves corresponded to points of high local strain, which could act as potential fatigue crack initiation sites. This observation further underlines the importance of the smooth surface finish achieved in HBT-FSW.

Macrographs of the fractured specimens (Fig. 13) reveal that SSBT-FSW failed within the SZ, close to the region of minimum hardness, consistent with previous studies. (Goebel et al., 2017). In contrast, BT-FSW and HBT-FSW exhibited failure along the transition between the SZ and the TMAZ. The failure observed in SSBT-FSW can be related to precipitation degradation, whereas in BT-FSW and HBT-FSW the fracture behaviour appears to be influenced by stress concentration arising from the microstructural mismatch at the SZ/TMAZ interface (Ji et al., 2020).

SEM analysis of the fracture surfaces, presented in Fig. 14 at various magnifications, confirmed predominantly ductile fracture behaviour for all welding variants. Secondary electron (SE) imaging, which provides topographical contrast, reveals that BT-FSW and HBT-FSW joints exhibit a high density of fine, uniformly distributed dimples, indicating more homogeneous plastic deformation. In contrast, SSBT-FSW exhibits fewer dimples and areas of quasi-cleavage, in line with its lower elongation at fracture. Backscattered electron (BSE) imaging, which provides compositional contrast with heavier elements appearing brighter, combined with EDS analysis, identifies Cu-rich Al_2Cu (θ) particles as void nucleation sites. The presence of coarser particles and larger voids in SSBT-FSW suggests earlier void nucleation and growth, explaining the lower elongation at fracture. The slightly higher elongation observed for BT-FSW and HBT-FSW can be attributed to their wider stir zones, which facilitate more distributed plastic deformation, as well as to a less degraded precipitate microstructure. These factors contribute to a more ductile fracture behaviour compared with SSBT-FSW at 150 mm/min.

4. Conclusions

This study introduces, for the first time, a new variant of BT-FSW, termed HBT-FSW. The increased heat input from the upper shoulder in HBT-FSW allows for higher welding speeds compared to SSBT-FSW, which had to be limited to 150 mm/min to prevent surface defects. The observed differences for SSBT-FSW reflect the influence of the reduced welding speed required to ensure defect-free welds.

Conventional BT-FSW joints exhibited micro-grooves from the rotating upper shoulder, along with moderate flash formation. In contrast, the SSBT-FSW and HBT-FSW variants produced smooth, flash-free surfaces owing to the ironing effect of the stationary upper shoulder. The removal of surface irregularities is therefore expected to reduce surface crack sensitivity and enhance fatigue life.

The reduced welding speed necessary for SSBT-FSW to prevent

surface defects led to the lowest hardness, which is attributed to pronounced precipitation overaging, as confirmed by the WAXS results. HBT-FSW displayed a microstructure comparable to BT-FSW in terms of grain size and precipitation evolution.

Tensile testing demonstrated that HBT-FSW achieved a yield strength of ~181 MPa, ultimate tensile strength of ~333 MPa, and elongation of ~5.3%, comparable to BT-FSW (~191 MPa, ~325 MPa, ~4.8%), whereas SSBT-FSW exhibited a lower elongation of ~3.9%. This decrease is attributed to a smaller stir zone resulting from lower energy input on the upper surface, as well as increased precipitate degradation due to the lower welding speed required to prevent surface defects. DIC analysis revealed that, in all cases, the highest strain and subsequent failure were localised on the AS. Fracture locations for HBT-FSW and BT-FSW were similar, occurring at the SZ/TMAZ transition, while for SSBT-FSW, the fracture was located within the stir zone.

Overall, the results demonstrate that the new HBT-FSW variant achieves welding speeds and mechanical properties comparable to BT-FSW, while maintaining the excellent surface quality characteristic of SSBT-FSW. This configuration has the potential to enhance manufacturing efficiency by allowing higher welding speeds without requiring post-weld machining of the upper surface. This represents a major advantage for industrial applications.

CRediT authorship contribution statement

Matteo Bernardi: Writing – review & editing, Writing – original draft, Visualization, Validation, Methodology, Investigation, Formal analysis, Data curation, Conceptualization. **Ting Chen:** Writing – review & editing, Writing – original draft, Visualization, Validation, Methodology, Investigation, Formal analysis, Data curation. **Mikael Guimaraes:** Writing – review & editing, Visualization, Validation, Investigation, Data curation. **Natã Lucas Beltrão da Silva:** Writing – review & editing, Validation, Investigation. **Juliano Marks:** Writing – review & editing, Validation, Investigation. **Guilherme N. Rezende:** Writing – review & editing, Validation, Investigation. **Pedro Jahn:** Writing – review & editing, Validation, Investigation. **Gabriela Gonçalves Gerevini:** Writing – review & editing, Validation, Investigation. **Emad Maawad:** Writing – review & editing, Visualization, Validation, Data curation. **Kai Schimanski:** Writing – review & editing, Project administration, Funding acquisition. **Damien Guilloteau:** Writing – review & editing, Project administration. **Manuel De Araujo:** Writing – review & editing, Project administration. **Marco Pacchione:** Writing – review & editing, Project administration, Funding acquisition. **Luciano Bergmann:** Writing – review & editing, Supervision, Project administration, Funding acquisition. **Benjamin Klusemann:** Writing – review & editing, Project administration, Funding acquisition.

Declaration of competing interest

The authors declare that they have no known competing financial interests or personal relationships that could have appeared to influence the work reported in this paper.

Acknowledgements

We would like to express our gratitude to the Deutsches Elektronen-Synchrotron DESY (Hamburg, Germany), which is a member of the Helmholtz Association HGF, for providing access to their experimental facilities. Data was collected using the P07B beamline operated by Helmholtz-Zentrum Hereon. We would like to thank Dr. Norbert Schell for assistance during the experiments. The work was carried out under grant numbers 20M2113H, 20M2113A, 20X2206G and 20X2206A, funded by the German Federal Ministry of Economic Affairs and Energy (BMWE) under the LuFo VI-2 and LuFo VI-3 programs. The authors would like to express their gratitude to Menno Peters, for his invaluable technical support throughout this work.

Appendix ASupplementary data

Supplementary data to this article can be found online at https://doi.org/10.1016/j.aime.2026.100190.

Data availability

Data will be made available on request.

References

Cabibbo, M., McQueen, H.J., Evangelista, E., Spigarelli, S., Di Paola, M., Falchero, A., 2007. Microstructure and mechanical property studies of AA6056 friction stir welded plate. Mater. Sci. Eng., A 460–461, 86–94. https://doi.org/10.1016/j.msea.2007.01.022.

Chan, C.Y.-C., Suhuddin, U.F.H.R., Maawad, E., Mordridge, M.T., Klusemann, B., 2025. Precipitation distribution in mechanically alloyed al-cu-li powders processed via friction consolidation. Mater. Des. 259, 114847. https://doi.org/10.1016/j.matdes.2025.114847.

Chen, G., Liu, S., Qin, Q., Chen, M., Jia, G., He, K., Zhang, H., 2025. Mechanism for enhanced strengthening due to pre-stretching of 2219 aluminum alloy. Mater. Sci. Eng., A 945, 148997. https://doi.org/10.1016/j.msea.2025.148997.

Chi, J., Song, H., Shao, H., Zhou, Y., Zheng, Q., Lu, N., Starostenkov, M.D., Dong, G., Bi, J., Tan, C., 2025. Inhibiting of softening behavior in AA2219 laser welded joints. Mater. Sci. Eng., A 924, 147742. https://doi.org/10.1016/j.msea.2024.147742.

Gao, Y., Chen, S., Chen, X., Li, X., Liu, Z., Dong, J., Zhao, P., 2025. Effect of rotating electromagnetic field on the microstructural evolution of 2219-T6 aluminum alloy during friction stir welding. J. Manuf. Process. 150, 714–725. https://doi.org/10.1016/j.jmapro.2025.06.040.

Goebel, J., Reimann, M., Norman, A., dos Santos, J.F., 2017. Semi-stationary shoulder bobbin tool friction stir welding of AA2198-T851. J. Mater. Process. Technol. 245, 37–45. https://doi.org/10.1016/j.jmatprotec.2017.02.011.

Gong, B.S., Zhang, Z.J., Wang, H.W., Liu, R., Liu, H.Z., Purcek, G., Demirtas, M., Yanar, H., Zhang, Z.F., 2025. Improving the fatigue limit of FSW6061 Al alloy welded joints by surface spinning rolling. Int. J. Fatig. 200, 109119. https://doi.org/10.1016/j.ijfatigue.2025.109119.

Hao, Y., Liu, W., 2022. Analysis on exceptional cryogenic mechanical properties of AA2219 alloy FSW joints in multi-scale. Mater. Sci. Eng., A 850, 143489. https://doi.org/10.1016/j.msea.2022.143489.

Henson, G., 2018. Materials for launch vehicle structures. In: Aerospace Materials and Applications, Progress in Astronautics and Aeronautics. American Institute of Aeronautics and Astronautics, Inc., pp. 435–504. https://doi.org/10.2514/5.9781624104893.0435.0504

Jata, K.V., Semiatin, S.L., 2000. Continuous dynamic recrystallization during friction stir welding of high strength aluminum alloys. Scr. Mater. 43, 743–749. https://doi.org/10.1016/S1359-6462(00)00480-2.

Ji, H., Deng, Y., Xu, H., Lin, S., Wang, W., Dong, H., 2020. The mechanism of rotational and non-rotational shoulder affecting the microstructure and mechanical properties of al-mg-si alloy friction stir welded joint. Mater. Des. 192, 108729. https://doi.org/10.1016/j.matdes.2020.108729.

Jiang, L., Rouxel, B., Langan, T., Dorin, T., 2021. Coupled segregation mechanisms of Sc, Zr and Mn at θ′ interfaces enhances the strength and thermal stability of Al-Cu alloys. Acta Mater. 206, 116634. https://doi.org/10.1016/j.actamat.2021.116634.

Keerti, S., Yang, X., Babu, N.H., 2025. A generic hall-petch relationship in metallic materials with varied grain morphology. Mater. Sci. Eng., A 943, 148764. https://doi.org/10.1016/j.msea.2025.148764.

Li, G., Chen, T., Fu, B., Shen, J., Bergmann, L., Zhou, L., Chen, K., dos Santos, J.F., Klusemann, B., 2023. Semi-stationary shoulder bobbin-tool: a new approach in tailoring macrostructure and mechanical properties of bobbin-tool friction stir welds in magnesium alloy. J. Mater. Process. Technol. 317, 117984. https://doi.org/10.1016/j.jmatprotec.2023.117984.

Li, X., Chen, S., Yuan, T., Jiang, X., Han, Y., 2020. Improving the properties of friction stir welded 2219-T87 aluminum alloy with GTA offset preheating. J. Manuf. Process. 51, 10–18. https://doi.org/10.1016/j.jmapro.2020.01.021.

Manikandan, P., Prabhu, T.A., Manwatkar, S.K., Rao, G.S., Murty, S.V.S.N., Sivakumar, D., Pant, B., Mohan, M., 2021. Tensile and fracture properties of aluminium Alloy AA2219-T87 friction stir weld joints for aerospace applications. Metall. Mater. Trans. 52, 3759–3776. https://doi.org/10.1007/s11661-021-06337-y.

Mishra, R.S., Ma, Z.Y., 2005. Friction stir welding and processing. Mater. Sci. Eng. R Rep. 50, 1–78. https://doi.org/10.1016/j.mser.2005.07.001.

Miyoshi, H., Kimizuka, H., Ishii, A., Ogata, S., 2021. Competing nucleation of single- and double-layer guinier–preston zones in Al–Cu alloys. Sci. Rep. 11, 4503. https://doi.org/10.1038/s41598-021-83920-8.

Perrin, T., Després, A., Heugue, P., Deschamps, A., Geuser, F.D., 2025. Investigation of the high thermal ageing resistance of the 2219 aluminium alloy. Mater. Des. 256, 114373. https://doi.org/10.1016/j.matdes.2025.114373.

Ramkumar, T., Selvakumar, M., Vasanthsankar, R., Sathishkumar, A.S., Narayanasamy, P., Girija, G., 2018. Rietveld refinement of powder X-ray diffraction, microstructural and mechanical studies of magnesium matrix composites processed by high energy ball milling. J. Magnesium Alloys 6, 390–398. https://doi.org/10.1016/j.jma.2018.08.002.

Reimann, M., Goebel, J., dos Santos, J.F., 2018. Microstructure evolution and mechanical properties of keyhole repair welds in AA 2219-T851 using refill friction stir spot welding. J. Mater. Eng. Perform. 27, 5220–5226. https://doi.org/10.1007/s11665-018-3519-z.

Rezende, G.N., Bernardi, M., Hoffmann, M., Bergmann, L., Zepon, G., Klusemann, B., 2025. Enhancement of the mechanical properties of semi-stationary bobbin tool friction stir welded joints in AA2219 through post-weld heat treatment. Mater. Sci. Eng., A 920, 147498. https://doi.org/10.1016/j.msea.2024.147498.

Shao, M., Wang, C., Zhang, H., Zhang, J., Liu, D., Wang, F., Ji, Y., Chen, G., 2022. Microstructure and corrosion behavior of bobbin tool friction stir welded 2219 aluminum alloy. Mater. Charact. 192, 112178. https://doi.org/10.1016/j.matchar.2022.112178.

Stobbs, W.M., Purdy, G.R., 1978. The elastic accommodation of semicoherent θ′ in Al 4wt.%Cu alloy. Acta Metall. 26, 1069–1081. https://doi.org/10.1016/0001-6160(78)90135-9.

Storm, M., Lotze, G., 2025. Pydidas - python diffraction data analysis suite. https://doi.org/10.5281/zenodo.15038277.

Wagner, D., Bernardi, M., Grassel, F., Chen, T., Schimanski, K., Bergmann, L., Klusemann, B., 2024. Analysis of mechanical properties and microstructure of single and double-pass friction stir welded T-joints for aluminium stiffened panels. Mater. Des. 247, 113438. https://doi.org/10.1016/j.matdes.2024.113438.

Wang, G., Zhao, Y., Hao, Y., 2018. Friction stir welding of high-strength aerospace aluminum alloy and application in rocket tank manufacturing. J. Mater. Sci. Technol. 34, 73–91. https://doi.org/10.1016/j.jmst.2017.11.041.

Wang, S.C., Starink, M.J., 2005. Precipitates and intermetallic phases in precipitation hardening Al–Cu–Mg–(Li) based alloys. Int. Mater. Rev. 50, 193–215. https://doi.org/10.1179/174328005X14357.

Wang, X., Zhang, F., Hu, D., Chen, R., Song, Z., 2023. Review, prospect and technical challenge of launch vehicle. In: Song, Z., Zhao, D., Theil, S. (Eds.), Autonomous Trajectory Planning and Guidance Control for Launch Vehicles. Springer Nature Singapore, Singapore, pp. 1–31. https://doi.org/10.1007/978-981-99-0613-0_1.

Wang, Z.L., Zhang, Z., Xue, P., Ni, D.R., Ma, Z.Y., Hao, Y.F., Zhao, Y.H., Wang, G.Q., 2022. Defect formation, microstructure evolution, and mechanical properties of bobbin tool friction–stir welded 2219-T8 alloy. Mater. Sci. Eng., A 832, 142414. https://doi.org/10.1016/j.msea.2021.142414.

Wolverton, C., Ozoliņš, V., 2001. Entropically favored ordering: the metallurgy of Al2 Cu Revisrted. Phys. Rev. Lett. 86, 5518–5521. https://doi.org/10.1103/PhysRevLett.86.5518.

Wu, H., Chen, Y.-C., Strong, D., Prangnell, P., 2015. Stationary shoulder FSW for joining high strength aluminum alloys. J. Mater. Process. Technol. 221, 187–196. https://doi.org/10.1016/j.jmatprotec.2015.02.015.

Yang, X., Meng, T., Su, Y., Qi, Z., Guo, Z., Wu, D., Ma, T., Li, W., 2024. Investigation on reducing residual stress and optimizing performance of 2219 aluminum alloy friction stir welded joint by cold spraying. J. Manuf. Process. 119, 87–97. https://doi.org/10.1016/j.jmapro.2024.03.068.

You, J., Li, J., Yang, M., Zhao, Y., 2025. Effect of rotational speed on constant pressure robotic friction stir welding: weld formation, microstructure, and mechanical properties. Mater. Today Commun. 49, 113802. https://doi.org/10.1016/j.mtcomm.2025.113802.

Zhang, T., Ji, H., Xu, D., Yin, X., Wei, H., Sun, Z., Liu, C., 2023. A hybrid shoulder to achieve a significant improvement in tensile strength and fatigue performance of friction stir welded joints for al–mg–si alloy. J. Mater. Res. Technol. 27, 2280–2291. https://doi.org/10.1016/j.jmrt.2023.10.067.